ADVANCED ENERGY MATERIALS
www.advenergymat.de

Silicon-Inspired Analysis of Interfacial Recombination in Perovskite Photovoltaics

*Sarah C. Gillespie, Jérôme Gautier, Julia S. van der Burgt, John Anker, Bart L.J. Geerligs, Gianluca Coletti, and Erik C. Garnett**

Perovskite solar cells have reached an impressive certified efficiency of 26.1%, with a considerable fraction of the remaining losses attributed to carrier recombination at perovskite interfaces. This work demonstrates how time-resolved photoluminescence spectroscopy (TRPL) can be utilized to locate and quantify remaining recombination losses in perovskite solar cells, analogous to methods established to improve silicon solar cell passivation and contact layers. It is shown how TRPL analysis can be extended to determine the bulk and surface lifetimes, surface recombination velocity, the recombination parameter, J_0, and the implied open-circuit voltage (iV_{oc}) of any perovskite device configuration. This framework is used to compare 18 carrier-selective and passivating contacts commonly used or emerging for perovskite photovoltaics. Furthermore, the iV_{oc} values calculated from the TRPL-based framework are directly compared to those calculated from photoluminescence quantum yields and the measured solar cell V_{oc}. This simple technique serves as a practical guide for screening and selecting multifunctional, passivating perovskite contact layers. As with silicon solar cells, most of the material and interface analysis can be done without fabricating full devices or measuring efficiency. These purely optical measurements are even preferable when studying bulk and interfacial passivation approaches, since they remove complicating effects from poor carrier extraction.

1. Introduction

The remarkable progress of perovskite solar cells in recent years has brought certified device efficiencies to >26% - within one percent of the silicon record.[1] Comparing record device parameters to the detailed balance (DB) limit, successful mitigation of the remaining losses should primarily proceed via further carrier management improvements (experimental records are ≈91% of the open-circuit voltage, V_{oc}, at DB, and ≈93% of the fill factor, FF, at DB), rather than from light management optimization (≈99% of the short-circuit current density, J_{sc}, at DB).[2–4] However it is not trivial to identify the significant carrier recombination pathways across the stack's layers based on device V_{oc} and FF readouts alone; supplemental characterization is generally required to locate and ultimately eliminate the major recombination losses to further improve device performance.

Particularly in the perovskite community, films, and half-fabricate cells are widely assessed using purely optical techniques. For example, the photoluminescence quantum yield (PLQY) and the minority carrier lifetime (τ) are frequently measured and included in perovskite photovoltaic reports.[5–9] These non-electrical assessment tools make it easier to compare film or half-stack quality without needing to fabricate full devices - but again these measurements alone will not answer the key question: are the carrier recombination losses coming from the bulk of the perovskite, from one or both of the perovskite-contact interfaces, or from somewhere else in the device? If this question is not addressed, the community may be misdirected to make erroneous assumptions and focus on optimizing regions within the stack which are already nearly perfect.

Conversely, the silicon PV community has been utilizing well-established techniques to isolate different recombination

S. C. Gillespie, J. Gautier, J. S. van der Burgt, E. C. Garnett
AMOLF Institute
Science Park 104, Amsterdam 1098XG, Netherlands
E-mail: e.garnett@amolf.nl

The ORCID identification number(s) for the author(s) of this article can be found under https://doi.org/10.1002/aenm.202400965

© 2024 The Author(s). Advanced Energy Materials published by Wiley-VCH GmbH. This is an open access article under the terms of the Creative Commons Attribution License, which permits use, distribution and reproduction in any medium, provided the original work is properly cited.

DOI: 10.1002/aenm.202400965

S. C. Gillespie, J. Anker, B. L. Geerligs, G. Coletti
TNO Energy Transition
Westerduinweg 3, Petten 1755LE, Netherlands

G. Coletti
School of Photovoltaic and Renewable Energy Engineering
University of New South Wales
Sydney, NSW 2052, Australia

E. C. Garnett
Institute of Physics
University of Amsterdam
Science Park 904, Amsterdam 1098XH, Netherlands

 © 2024 The Author(s). Advanced Energy Materials published by Wiley-VCH GmbH

processes for the past 30 years.[10–13] Specifically, the photoconductance decay method enables the fast and simple determination of the minority carrier lifetime - similar to what is typically extracted from time-resolved photoluminescence (TRPL) decays for perovskite films. With the lifetime easy to quantify, further methods such as thickness-variation measurements have enabled the separation of bulk and surface recombination contributions in silicon and germanium wafers.[14–16] Moreover, it is typical for the silicon community to quote the recombination current density J_0 or the implied open-circuit voltage, iV_{oc}, of the wafer rather than its minority carrier lifetime.[17–19] Reporting these parameters can be exceedingly more practical than reporting lifetime alone as they can easily be compared to the properties of the equivalent device's current–voltage curve.

Herein, we propose a framework to experimentally locate and separate the non-radiative Shockley-Read-Hall (SRH) recombination processes as they occur across any perovskite stack, with inspiration drawn from the longstanding silicon techniques. This framework emphasizes how one can extend from the archetypal time-resolved photoluminescence spectroscopy measurements to separate bulk and surface recombination losses at either interface. We describe how the surface recombination velocity (SRV) can be extracted at either contact by measuring τ_{eff} as a function of perovskite thickness, W_{pvk}, provided the carrier diffusion length is known.[14,20] Using this framework, this work provides the experimentally-determined SRVs of 18 different passivating and carrier selective contacts with the $Cs_{0.06}(MA_{0.2}\ FA_{0.8})_{0.94}$ Pb $(Br_{0.2}\ I_{0.8})_3$ perovskite.[21] We further compare SRVs when the perovskite stack is inverted.

We continue by explaining the utility of using the recombination parameter J_0 and the separated bulk and surface J_0 components either in addition to, or instead of, quoting the SRV or PLQY in reports. In line with the argument that determining the J_0 can aid in the understanding of solar cell performance, we finish by detailing how the implied V_{oc} extracted from the proposed framework compares to the implied V_{oc} extracted from PLQY, and to the true V_{oc} measured for full devices, highlighting the losses predicted from the framework analysis and losses from other sources not included in the analysis. Experimentally, we determine that the limiting region due to SRH recombination in our solar cells is at the perovskite-C_{60} interface, which accounts for ≈90% of the total non-radiative open-circuit voltage losses. We further show that for perfectly passivated cells, the maximum iV_{oc} that can be achieved is ≈1.29 V, signifying that the perovskite bulk quality is already exceptionally high in this case.

Finally, we show in this work that reporting full device efficiencies is not strictly necessary for analyzing current and next-generation perovskite contact layer passivation properties. Indeed, we argue that focusing on high efficiencies alone can be detrimental to perovskite solar cell progress as, even with a high quality perovskite active layer and state-of-the-art contacts, device efficiencies can remain limited due to hidden additional losses. Without a separate analytical procedure in place to identify and quantify each loss process, device optimization can be limited. This argument has already been established in the silicon community - here we simply extend the rationale to perovskite photovoltaics.

2. SRH Recombination and the Minority Carrier Lifetime for PV Materials

Deviation from the detailed balance limit for any trap-containing photovoltaic material is, by definition, partially attributed to trap-assisted SRH recombination, which can occur within the bulk of the material or at its surface, depending on the location and nature of the trap.[3,22] For perovskite solar cells in particular, SRH recombination is still a major energy loss pathway that limits device efficiencies.[23,24] Consequently, the material quality of any photovoltaic layer can be quantified by determining the SRH recombination rate, which is proportional to the trap density in the material. By means of convention, it is not the SRH recombination rate, R_{SRH}, that is quoted and compared in literature, but the effective SRH lifetime - a proxy of the inverse recombination rate, given as:

$$\tau_{SRH,eff} = \frac{\Delta n}{R_{SRH}} \tag{1}$$

for p-type semiconductors ($\tau\tau_{SRH,\,eff} = \Delta p / R_{SRH}$ for n-type semiconductors). The effective SRH lifetime, shortened to τ_{eff} is related to the SRH bulk and SRH surface lifetimes by:

$$\frac{1}{\tau_{eff}} = \frac{1}{\tau_{bulk}} + \frac{1}{\tau_{surf}} \tag{2}$$

Separation of these lifetimes and further analysis will be described in Sections 3 and 4. Before that, it is first necessary to discuss the standard methods applied to determine the effective lifetime. While experimental methods can vary between photovoltaic materials, such as between silicon and perovskite samples, the underlying theory and the lifetime meaning are the same.

2.1. Measuring the Minority Carrier Lifetime in Silicon Wafers

In silicon photovoltaics, the effective minority carrier lifetime of a wafer is generally determined using the photoconductance decay technique. This technique, for the near majority of researchers and industrial testers, is carried out using the Sinton WCT-120 assessment tool.[10,11] To illustrate this technique, we fabricate and measure the lifetime of an n-type Czochralski silicon wafer with symmetric nitric acid oxidized silicon (NAOS) tunneling layers and with 20 nm of n-type polysilicon deposited symmetrically on top the oxide (fabrication details are listed in the Supporting Information).

In the measurement, the symmetric n-poly/SiO_2/silicon wafer is placed on top of the induction coil and a flash from a standing lamp briefly illuminates the wafer, as schematically shown in **Figure 1a**. The raw photovoltage decay is measured as a function of time (Figure 1b) and is converted to the photoconductance decay ($\Delta\sigma_G$) based on a predefined calibration curve of the induction coil.[12] The excess carrier concentration as a function of time is then obtained based on the relation: $\Delta\sigma_G = qW\Delta p(\mu_n + \mu_p)$, where mobilities are known for silicon (typically, electron mobilities are μ_n ≈1100 $cm^2V^{-1}s^{-1}$ and hole mobilities are μ_p ≈400 $cm^2V^{-1}s^{-1}$), and the thickness is a measured input - in this case, W_{Si} = 180 µm.[11]

© 2024 The Author(s). Advanced Energy Materials published by Wiley-VCH GmbH

16146840, 0, Downloaded from https://onlinelibrary.wiley.com/doi/10.1002/aenm.202400965 by Cochrane Netherlands, Wiley Online Library on [14/08/2024]. See the Terms and Conditions (https://onlinelibrary.wiley.com/terms-and-conditions) on Wiley Online Library for rules of use; OA articles are governed by the applicable Creative Commons License

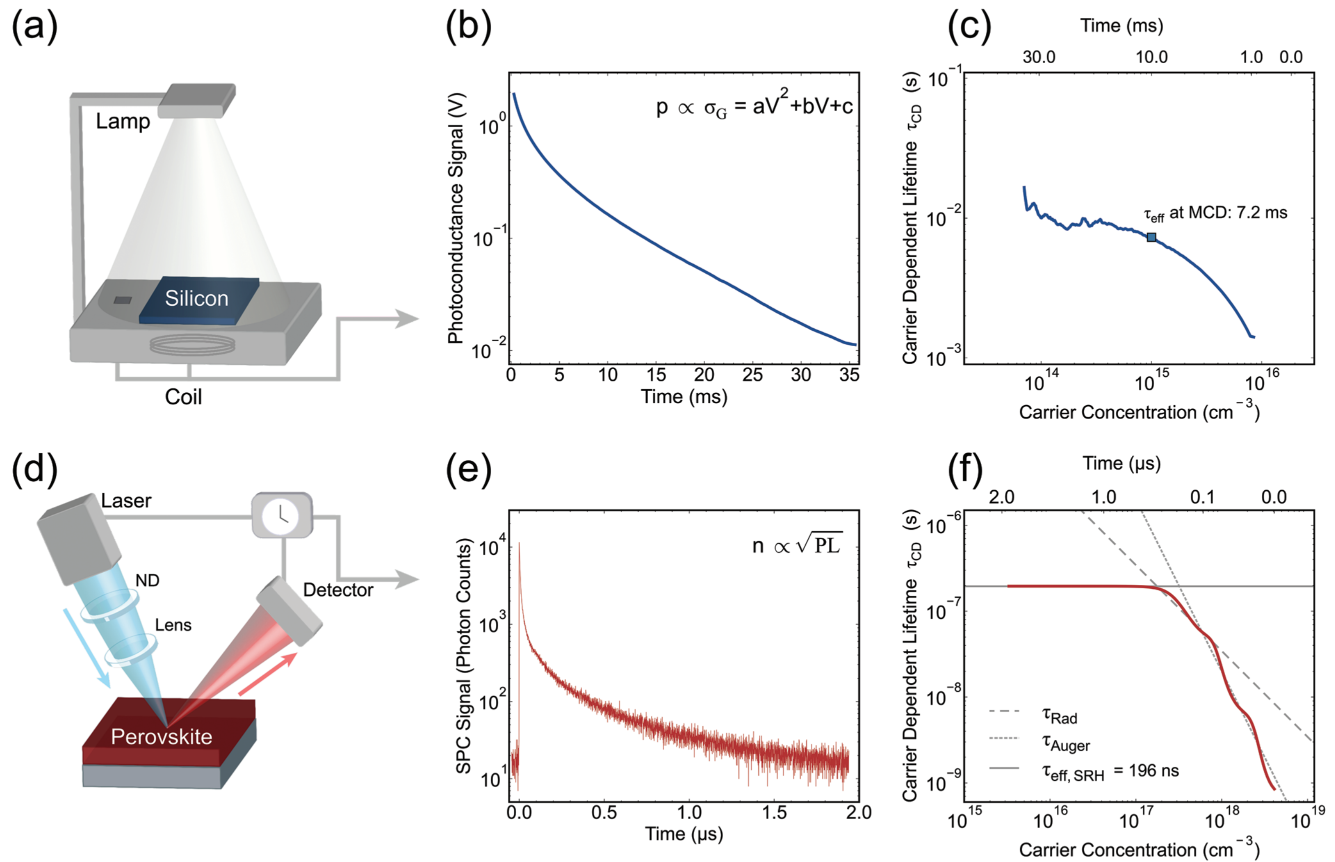

Figure 1. a) Schematic of the Sinton WCT-120 lifetime assessment tool for silicon PV. b) The raw photovoltage decay signal as a function of time for the symmetric n-poly Si/SiO_2 on n-Si wafer. c) Determined carrier-dependent lifetime as a function of carrier concentration (primary x-axis) and as a function of time (secondary x-axis), calculated from Equation 4. The reported τ_{eff} is at the standard MCD of 10^{15} cm^{-3}. d) Schematic of the typical TCSPC lifetime set-up for TRPL measurements. In this work, λ_{ex} = 485 nm ($\lambda_{em} \approx$ 780 nm after ≈2 min of steady-state excitation). e) The cumulative photon signal collected over time for the perovskite on glass sample. f) Carrier-dependent lifetime (differential lifetime) as a function of carrier concentration and as a function of time, calculated from Equation (6). τ_{eff} is determined at the saturation point of the curve, which is defined to be at the SRH limit. The radiative carrier lifetime (dashed) and Auger carrier lifetime (dotted) are also plotted based on our fit and on reported coefficients for a similar perovskite composition; $k_{Rad} = 2.9 \times 10^{-11}$ cm^{-3}s^{-1}, $C_{Auger} = 5 \times 10^{-29}$ cm^{-6}s^{-1}.[38,39]

The effective carrier lifetime can then be obtained using the standard continuity equation with the assumption that the carrier concentration is spatially uniform across the sample. Under this assumption, the continuity equation is reduced to:

$$\frac{d\Delta p(t)}{dt} = G(t) - R(t) \tag{3}$$

where $G(t)$ and $R(t)$ are the total time-dependent carrier generation and recombination rates, respectively. There are three analysis modes that can be selected based on the expected lifetime.[13] For high quality and well-passivated wafers, the transient mode is most commonly applied - used when the carrier lifetime of the symmetric silicon sample is longer than the flash time. Under this condition, $G(t) \approx 0$ can be assumed and the continuity equation simply becomes:

$$\tau_{CD}(\Delta p) = -\frac{\Delta p}{d\Delta p(t)/dt} \tag{4}$$

Wherein the variable or 'carrier-dependent' lifetime is defined as:

$$\frac{1}{\tau_{CD}} = \frac{1}{\tau_{eff}} + \frac{1}{\tau_{Radiative}} + \frac{1}{\tau_{Auger}} \tag{5}$$

We plot the carrier-dependent lifetime both as a function of carrier concentration and of time for our illustrative silicon sample in Figure 1c. Conventionally, the reported lifetime is given at the minority carrier density (MCD) corresponding to one-tenth of the wafer doping density (N_D), typically at 10^{15} cm^{-3}.[25] In our case, τ_{CD}@MCD = 7.2 ms, as indicated by the blue marker in Figure 1c. This marker is located approximately at the plateau of the carrier-dependent lifetime curve, which is an indication that SRH is the dominant recombination process - signifying that at this point, $\tau_{CD} \approx \tau_{eff}$. Indeed, this is the underlying justification of reporting lifetimes at $0.1 \times N_D$. At higher carrier concentrations, τ_{CD} is much shorter, which is of course the consequence of radiative and Auger recombination processes becoming increasingly dominant.[26]

© 2024 The Author(s). Advanced Energy Materials published by Wiley-VCH GmbH

16146840, 0, Downloaded from https://onlinelibrary.wiley.com/doi/10.1002/aenm.202400965 by Cochrane Netherlands, Wiley Online Library on [14/08/2024]. See the Terms and Conditions (https://onlinelibrary.wiley.com/terms-and-conditions) on Wiley Online Library for rules of use; OA articles are governed by the applicable Creative Commons License

2.2. Measuring the Minority Carrier Lifetime in Perovskite Films

Comparatively, in perovskite photovoltaics, the carrier lifetime is typically determined by using time-correlated-single-photon-counting (TCSPC) to obtain the PL decay trace.[27] We similarly provide an illustrative case by measuring the PL decay of the $Cs_{0.06}(MA_{0.2}\ FA_{0.8})_{0.94}\ Pb\ (Br_{0.2}\ I_{0.8})_3$ perovskite on glass. In the standard TCSPC experimental procedure, which is schematically shown in Figure 1d, a pulsed laser excites the film and an emitted photon from the sample is detected some time later typically with a single photon counter. The time of travel of the photon to the detector is subtracted such that only the time difference between excitation and emission is recorded. This process is repeated several million times to build up a histogram of the decay curve, shown in Figure 1e. Notably, the repetition rates, RR, for all TRPL measurements in this work were selected by ensuring that $\tau_{eff} \ll RR^{-1}$. This ensures that in every case the full decay was captured.[28–30]

In many works, researchers generally obtain the minority carrier lifetime by fitting a nth order (usually n = 2) exponential to the TRPL decay: $PL(t) = \sum_{i=1}^{n} A_i \exp(-t/\tau_i)$. Generally, the long lifetime obtained from the fit is quoted as the effective minority carrier lifetime, since the solution to the continuity equation at the SRH limit is a monoexponential decay.[31–33] However, there are some nuances in fitting such an arbitrary function to the decay, namely that while the solution of the continuity equation for the SRH component is a monoexponential, other processes – radiative, Auger, extraction, re-injection, and so forth – generally are not, making the biexponential fitting procedure quite groundless. This has already been eloquently described in other works.[34,35] In the same works, it has instead been proposed that the 'differential lifetime':

$$\tau_{diff}(\Delta n) = -\left(\frac{d \ln \Delta n(t)}{dt}\right)^{-1} = -\left(\frac{1}{2}\frac{d \ln PL(t)}{dt}\right)^{-1} \tag{6}$$

should be used to analyze TRPL decays to find the more accurate effective SRH lifetime (it is assumed in this work that the perovskite layer is p-doped). The factor of 2 in Equation (6) arises from measuring under high injection levels, PL $\propto n^2$. By the differential lifetime definition, the point of saturation of the differential lifetime is the effective lifetime, provided no other injection or extraction processes are occurring and that first order radiative recombination is negligible. It is noted that while there has already been some adoption of applying differential lifetime technique for TRPL analysis, it has not yet been heavily popularized.[36–38]

In this work, we apply the differential lifetime analysis technique to extract the effective lifetime of the perovskite sample. The differential lifetime - for sake of comparison, redefined as the carrier-dependent lifetime - of the illustrative perovskite sample is plotted as function of carrier concentration and as a function of time in Figure 1f. The carrier concentration of the perovskite, shown along the primary x-axis in Figure 1f, is not directly measured but approximated using the laser fluence, laser spot size, film thickness and absorption, as described in the Supporting Information. From the plateau of the curve, the effective lifetime of the perovskite sample is τ_{eff} = 196 ns. Similar to the silicon lifetime analysis, the drop off in the carrier-dependent lifetime is as a consequence of radiative and Auger recombination dominating at high carrier concentrations. We exemplify this by also plotting the radiative and Auger lifetimes as a function of minority carrier concentration in Figure 1f, which we determine in this work by simply fitting the curve to Equation (5) and noting that the extracted values strongly agree with the reported values of a similar perovskite composition.[38] The figure highlights that radiative recombination accounts for the carrier-dependent lifetime transition at 2×10^{17} cm^{-3} $< \Delta n < 10^{18}$ cm^{-3}, while Auger dominates at $\Delta n > 10^{18}$ cm^{-3}. It is noted that, upon illumination, the effective Auger and radiative lifetimes will vary over time due to local material changes such as halide segregation occurring within the film; we further discuss such variations and the effect on the shape of Figure 1f in the Supporting Information.

We provide one final note regarding the effective lifetime determination for perovskite films in this work: we measure samples only under high injection level conditions, in which case the effective lifetime is the sum of the electron and hole lifetimes, $\tau_{eff} = \tau_p + \tau_n$. For low injection levels, the plateau would correspond to either τ_p or τ_n, depending on the polarity of the dopant; the low injection lifetime (assumed to be τ_n) of this perovskite on glass example is reported and further discussed in the Supporting Information.

3. Separating Bulk from Surface Recombination Processes

3.1. Thickness-Dependent Effective Lifetime Measurements

We now return to Equation (2) and discuss the means of separating the bulk from surface recombination processes from the measured effective lifetime. While the bulk lifetime is a reasonably straightforward and understandable parameter to characterize the bulk quality of perovskite films, the surface lifetime is not. This is due to the fact that the surface lifetime depends on more than simply the rate of SRH recombination at the surface; it also depends on the layer thickness and carrier diffusivity, both of which can of course vary between samples. It is therefore more appropriate to determine and quote the surface recombination velocity, which depends only on the surface properties, such as the surface trap density and the carrier concentration at the surface.[40]

Relating the surface lifetime to SRV has previously been outlined in literature and that study noted that a direct relation is not trivial - the generalized form can only be solved numerically.[20] However, the boundary conditions can be approximated analytically, which provide upper and lower limits to the determined SRV. Defining the effective SRVs of either interface to be S_1 and S_2, we can write that at the limit wherein $S_1 \gg S_2$ ($S_2 \approx 0$):

$$\tau_{surf} = \frac{2W}{S_1} + \frac{4}{D}\left(\frac{W}{\pi}\right)^2 \tag{7}$$

For the limit of $S_1 = S_2$, the relationship is approximated as:

$$\tau_{surf} = \frac{2W}{S_1 + S_2} + \frac{1}{D}\left(\frac{W}{\pi}\right)^2 \tag{8}$$

© 2024 The Author(s). Advanced Energy Materials published by Wiley-VCH GmbH

16146840, 0, Downloaded from https://onlinelibrary.wiley.com/doi/10.1002/aenm.202400965 by Cochrane Netherlands, Wiley Online Library on [14/08/2024]. See the Terms and Conditions (https://onlinelibrary.wiley.com/terms-and-conditions) on Wiley Online Library for rules of use; OA articles are governed by the applicable Creative Commons License

In the above expressions, W is the thickness of the photoactive layer and D is the ambipolar diffusion constant (under high injection levels). The factor of 2 in each of the first terms arises from the assumption that the effective SRV at either interface, S, is equivalent to both the hole SRV and electron SRV - that is, $S_e + S_h = 2S$.[35]

For perovskite materials, several works argue that as the carrier diffusion length (related to D by $L_d = \sqrt{D\tau}$) is much longer than the typical film thickness, so the second term in Equations (7) and (8) is negligible.[34,35,41,42] This assumption would enable the convenient case of:

$$\tau_{surf} \approx \frac{2W}{S_1 + S_2} \tag{9}$$

This assumption can be somewhat justified on the basis that there are many reports finding L_d to be at least 5 µm for polycrystalline perovskite thin films.[43–46] However, the true diffusion length of any perovskite film depends on a myriad of factors including polycrystallinity and chemical composition. Consequently, mixed halide perovskite films have been reported in other works to have diffusion lengths much closer to the typical film thickness.[47–50] To this extent, we argue that this assumption should be approached with caution; in any case, entirely neglecting the diffusivity term and still obtaining reasonable surface lifetimes only holds for relatively low SRVs.

To ascertain whether the second term can be omitted to simplify our analytical procedures, we solve for the effective lifetime when either Equations (7) or (8) are used to find τ_{surf}, and compare the results to when Equation (9) is used to find τ_{surf}. We present the results in Figure S10 (Supporting Information). In the Supporting Information, we also discuss the limiting scenarios for when the diffusivity term is necessary for a range of different SRVs and diffusion lengths. Based on the experimentally obtained effective lifetimes in this work and comparing with the analytical results, we deduce that the transverse carrier diffusion length must be $\geqslant$1 µm. We supplement this calculation by experimentally measuring the lateral carrier diffusion length of our triple cation mixed halide perovskite thin film on glass using a home-built steady-state photocarrier grating (SSPG) set up, the experimental details of which are described in our previous work.[51] Typically for perovskite films, the transverse carrier diffusion length is significantly longer than the lateral diffusion length.[52] From these measurements, we obtain an in-plane carrier diffusion length of $L_{d,\,lat} \approx 500$ nm.

With the diffusion length considered, it is now reasonable to confirm and utilize the relationship of the effective lifetime with surface recombination velocities and bulk lifetime:

$$\frac{1}{\tau_{eff}} = \frac{1}{\tau_{bulk}} + \frac{S_1 + S_2}{2W_{pvk}} \tag{10}$$

Drawing inspiration from similar techniques applied in the silicon community, we separate the bulk from surface recombination parameters by varying the thickness of unencapsulated perovskite films on glass and plot the inverse effective lifetime as a function of the inverse thickness in **Figure** 2a.[14–16] Using Equation (10), the inverse intercept from the fit is τ_{bulk} and the slope is $(S_{air} + S_{glass})/2$. The unencapsulated perovskite linear fit yields a bulk lifetime of $\tau_{bulk} \approx 1$ µs. However, as the associated statistical uncertainty of the intercept is high (± 4 µs, as depicted as the gray region Figure 2a), there are clearly issues with this initial approximation, which we attribute to ongoing interfacial reactions such as oxidation occurring at the perovskite-air interface. To reduce the associated uncertainty, we further measure the effective lifetime as a function of thickness for both perovskite films encapsulated in trioctylphosphine oxide (TOPO, shown in green), and e-beam evaporated SiO_2-encapsulated perovskite films (shown in red). As presented in Figure 2a, the spread of data, thereby the associated uncertainties of the intercepts, are in both cases reduced. This allows for a better approximation of τ_{bulk} to be obtained. We determine from the TOPO-encapsulated dataset that $\tau_{bulk} \approx 2 \pm 1$ µs.

Furthermore, as TOPO has been shown to passivate the dangling bonds incredibly well when deposited on top of perovskite films, the SRV of the perovskite-TOPO interface is near zero, allowing one to determine the SRV of the rear perovskite-glass interface as simply twice the slope of the best linear fit.[35,42,53] The SRV of the perovskite-glass interface was determined to be $S_{glass} = 200 \pm 80$ cms^{-1}. This is in agreement with the slope from the SiO_2-encapsulated dataset ($S_{glass} = 300 \pm 150$ cms^{-1}), the latter calculated with the assumption that the SRVs of the top and rear SiO_2 interfaces are equal. Using the former value for S_{glass}, the SRV between the perovskite and air can also be determined: $S_{air} = 1100 \pm 500$ cms^{-1}.

This thickness-variation method can be applied for all perovskite structures of interest and, particularly when using encapsulants such as TOPO or SiO_2, the bulk lifetime and the SRVs become experimentally straightforward to obtain. Moreover, if the assumption is made that the perovskite bulk carrier lifetime does not substantially differ when deposited on different contacts, one can then use the bulk lifetime obtained from the fits in Figure 2a and extend to rapidly obtain the SRV of layers, which are of greater interest in the photovoltaic community. We highlight that such an assessment has already been implemented for the extraction of the SRVs of several selective contacts on $MAPbI_3$ films in the past.[42] The assumption that bulk lifetime does not drastically change is somewhat reasonable considering that, while the bulk lifetime does tend to slightly differ when the perovskite film is formed over different substrates, it does not span orders of magnitude and it furthermore has been shown in literature the bulk rarely limits the measured effective lifetime.[41,49,54] As a result, the extracted values for τ_{bulk} and S_{air} (or indeed S_{glass} if SiO_2-encapsulation is applied) can be used to then determine the $S_{contact}$, the SRV of the rear contact, using the above relations.

3.2. Experimental Determination of SRV for PV-Relevant Contacts

The effective lifetimes of the substrate-contact-perovskite stacks were measured for 18 different thin contacts of interest for photovoltaic applications. The SRVs of the seven hole transport layers (HTLs), seven electron transport layers (ETLs) and four additional materials were then obtained using Equation (10) and the predetermined τ_{bulk} and S_{air} values, with the uncertainty range determined from the limits of $S_1 \gg S_2$ and $S_1 = S_2$. The effective lifetimes and corresponding SRVs are plotted in Figure 2b.

© 2024 The Author(s). Advanced Energy Materials published by Wiley-VCH GmbH

16146840, 0, Downloaded from https://onlinelibrary.wiley.com/doi/10.1002/aenm.202400965 by Cochrane Netherlands, Wiley Online Library on [14/08/2024]. See the Terms and Conditions (https://onlinelibrary.wiley.com/terms-and-conditions) on Wiley Online Library for rules of use; OA articles are governed by the applicable Creative Commons License

16146840, 0, Downloaded from https://onlinelibrary.wiley.com/doi/10.1002/aenm.202400965 by Cochrane Netherlands, Wiley Online Library on [14/08/2024]. See the Terms and Conditions (https://onlinelibrary.wiley.com/terms-and-conditions) on Wiley Online Library for rules of use; OA articles are governed by the applicable Creative Commons License

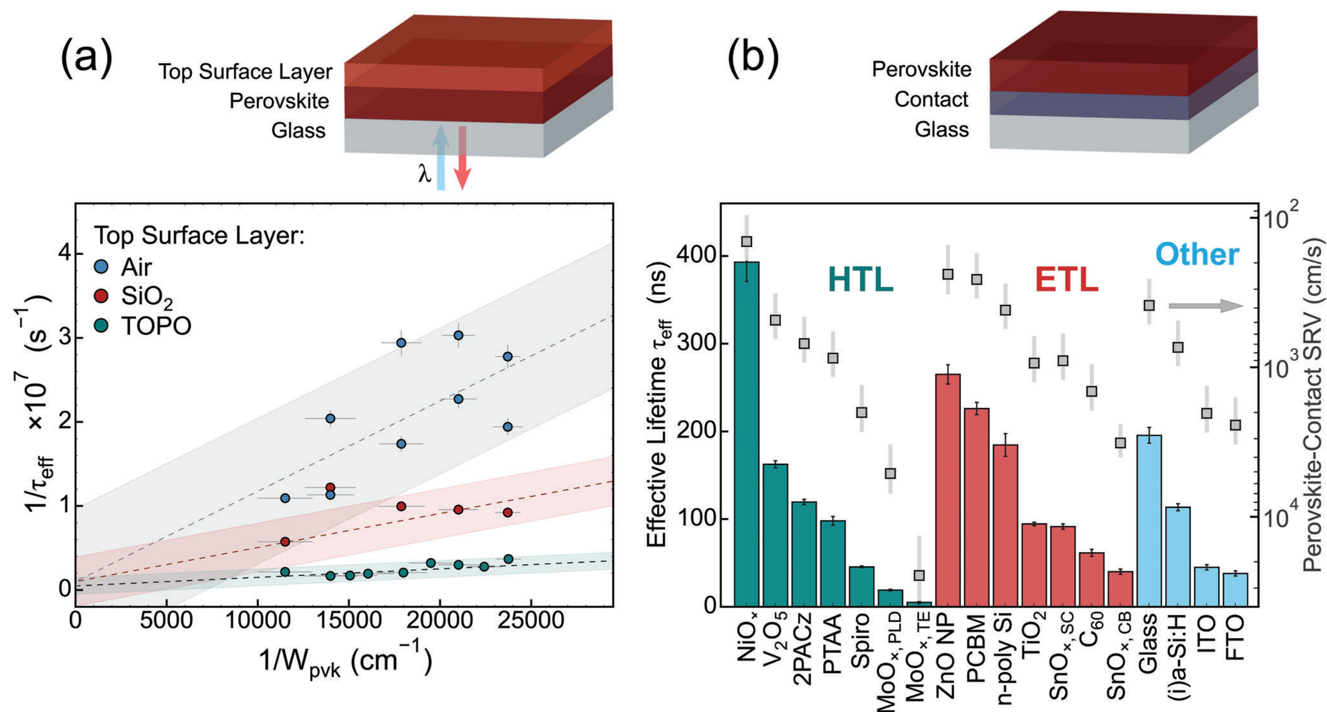

Figure 2. a) Above: schematic depicting the standard sample configuration used for thickness dependent lifetime measurements. The blue and red arrows indicate the direction of laser excitation and collected PL emission, respectively. Below: the inverse effective lifetime as a function of inverse perovskite thickness, with linear fits applied to the data (dashed lines). The fits were used to determine the bulk lifetime (intercept^{-1}) and the surface recombination velocities ($S_1 + S_2 = 2 \times$ slope) for unencapsulated perovskite films (blue), SiO_2-encapsulated films (red) and TOPO-encapsulated films (green). The shaded regions correspond to the statistical uncertainty of the fitted intercept. All perovskite films were fabricated on glass substrates. b) Above: schematic of the sample configuration applied to determine SRVs of the PV-relevant contacts. Below: corresponding histogram of the effective carrier lifetimes (read from the left y-axis) measured for 18 different contacts of interest, grouped into HTLs (green), ETLs (red) and remaining contacts not typically used as transport layers (blue). The corresponding determined SRVs for each contact are shown as the gray markers and read from the right y-axis. The gray errorbars indicate the SRV range determined from the boundary conditions defined from Equations (7) and (8).

The extracted SRV values are of course sensitive to the nature of the perovskite (composition, deposition, method, treatment) - as such, different works may report slightly different values. However, despite the compositional variation, it is emphasized that the SRVs determined in this work are in agreement with the SRVs of similar contacts but on $MAPbI_3$ films.[42]

We first emphasize the caveats of directly measuring the passivation of a contact with the intent of relating the results to a full device. By inspecting the graph, one notes that in particular NiOx, deposited as Ni by e-beam evaporation followed by high-temperature annealing in air, exhibits by far the lowest SRV of ≈80 cms^{-1}. From purely a passivation viewpoint, one would expect NiOx to serve as the most effective HTL under a single junction pin configuration. It is however emphasized that passivation does not automatically infer effective carrier extraction; poor band alignment or the formation of a passivating inert layer by redox reactions at the oxide-perovskite interface will, and do, limit effective carrier extraction.[55] Indeed, in our previous work we found that the NiOx interface was limiting the performance in our back-contact perovskite solar cells, due to the formation of a large carrier extraction barrier.[9] As a second caveat, significant variations from the perovskite-glass reference should be tracked with supplemental optical and morphological characterization, such as with x-ray diffraction (XRD), scanning electron microscopy, absorption spectroscopy and PL (all of which are presented in the Supporting Information). Should significant deviations occur for a test sample compared to the glass reference - for example if an excess of PbI_2 is present, determined from XRD, it is recommended that a thickness-dependent effective lifetime dataset is collected for that sample, and the SRV is extracted instead from the slope. With the caveats known, we argue that this method serves as a reasonable and efficient screening technique to determine the passivation properties of any contact located on the rear of the perovskite film.

In addition to directly comparing the passivation performance of different contact materials using this technique, the influence of deposition method can also be established. For example, we compare 10 nm films of MoOx, deposited by either pulsed laser deposition (PLD) or by thermal evaporation (TE).[56] As shown in Figure 2b, the passivation of $MoOx_{TE}$ (SRV ≈2.5×10^4 cms^{-1}) is much worse than that of $MoOx_{PLD}$ (SRV ≈5.1×10^3 cms^{-1}). Similarly, we show that the surface recombination of the SnOx ETL is higher when fabricated using chemical bath deposition (SRV ≈2.3×10^3 cms^{-1}) compared to the standard spin-coating method (SRV ≈900 cms^{-1}).[5]

Furthermore, we can apply this method to screen for prospective passivating, carrier selective contacts for single junction and tandem perovskite devices. The case in point for this work is highlighted with the SRV measurements of intrinsic amorphous

© 2024 The Author(s). Advanced Energy Materials published by Wiley-VCH GmbH

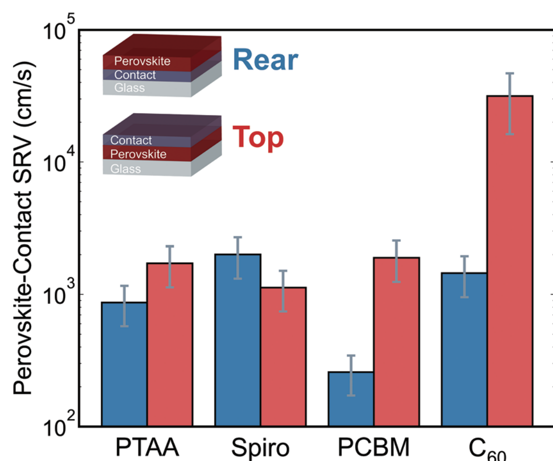

Figure 3. The difference in the measured SRV of perovskite-PTAA, -Spiro, -PCBM and -C_{60} interfaces when the contacts are deposited at the rear (blue) or on top (red) of the perovskite film.

silicon, (i)a-Si:H, and n-type polysilicon (n-poly Si) - both are comparable to state-of-the-art perovskite contacts.

As the SRV of the perovskite-glass substrate interface is known, it is evident that the contact position in the stack can be inverted, enabling one to also obtain the SRV of the contact when it is employed as a superlayer rather than a sublayer. This extends the applicability of this technique, enabling us to compare different contacts under realistic device configurations. We select four common contacts of interest, namely the HTLs of Spiro-OMeTAD (Spiro) and PTAA, and the ETLs of C_{60} and the related PCBM. These contacts were selected as they are quite extensively used as typical transport layers in perovskite solar cells, and they additionally can be easily spin-coated or evaporated either on the substrate or on the perovskite film without major sample alterations. It is widely known that PTAA and C_{60} are preferentially utilized in the pin configuration, while Spiro and PCBM are generally utilized in the nip configuration.[57,58] With the exception of the high SRV of C_{60} when deposited on top of the perovskite layer, we find that such common preferential configurations agree with the differences in our experimentally determined SRVs, which we compare in **Figure 3**.[59,60] The underlying reasons for differing SRV values between the same contacts but with an inverted stack order are complex. We propose that a key reason is likely due to the different nucleation and growth mechanisms of the deposited layers, which are highly dependent on the substrate beneath; such surface variability has been shown to occur for perovskite films grown upon different substrates.[54,61] We further postulate that dry deposition methods, such as evaporation, will likely lead to less intermixing of the contacts at the surface compared to wet processing methods. Whether this intermixing is beneficial or detrimental for the device likely depends on the precise contact composition.

The determination of the SRV of any contact regardless of their position in the perovskite stack enables one to calculate the effective total SRV for any hypothetical perovskite configuration i.e., with any two contacts placed on either side of the film. The benefit of this calculation is that it can then be converted to the corresponding upper limit for the open-circuit voltage, provided that extraction beyond the carrier transport layer is perfect. These calculations can therefore be used to determine and optimize the limiting contact(s) in current and next-generation perovskite photovoltaic devices, and further indicate whether additional significant losses occur beyond carrier extraction and separation into the transport layers.

4. Open-Circuit Voltage Predictions and Solar Cell Comparisons

We now focus on addressing the question: how do the SRH recombination properties, determined using the above methodology, translate to full device open-circuit voltages and cell efficiencies? To address this relationship, we first consider the simple perovskite half-stack configuration schematically portrayed in the upper half of Figure 2b.

We begin by assessing whether the extracted SRVs agree with a second material property that directly relates to the minority carrier recombination - the PLQY. As the PLQY is simply the ratio of the radiative to total recombination rate in a semiconductor material, it is inversely proportional to the non-radiative recombination rate and, by extension, the measured SRV of the same sample. We exemplify this relationship by plotting the inverse percentage PLQY against the perovskite-contact SRV for a subset of 11 contacts in **Figure 4a**. We omit FTO, ITO, the silicon-based contacts, MoOx and $SnOx_{CB}$ as these contacts currently are not widely applied directly as an interfacial layer to the perovskite film in PV technologies. With the exception of two outliers, the samples which consider Spiro and V_2O_5, the results follow the expected inverse linear relationship. These outliers can be attributed to degradation between measurements and local differences on the samples. Specifically in the case of Spiro, the wettability of the perovskite was poor on the contact which in turn implied regional differences in the film formation and quality (this argument is supported by the low solar cell performance which is shown later in this section).

While the conversion from the measured PLQY to the sample's implied open-circuit voltage is relatively straightforward - simply $iV_{oc} = V_{oc,\,Rad} + V_{therm} \ln(PLQY)$, where V_{Rad} is the open-circuit voltage at the radiative limit and V_{therm} is the thermal voltage (25.85 mV) - the direct relationship between the minority carrier lifetime and open-circuit voltage is slightly more nuanced. We will consider an approach with two variations in converting τ_{eff} to iV_{oc}: the first variation is that we directly apply a previously derived expression specifically for perovskite materials and their properties.[28] The second variation is by more generally converting the SRH recombination parameters first to their corresponding J_0 values and summing all the recombination components.[62] Of course, both of these variations are derived from first principles - as such they should yield the same result (this is verified in the Supporting Information). However, each calculation relies on different perovskite properties; the variation one chooses will simply depend on which properties are known.

Beginning with the first method, it has previously been shown that the iV_{oc} can be determined from τ_{eff}, provided that the background doping density, N_A, the carrier generation rate G, the radiative recombination coefficient k_{Rad}, the probability of escape (P_e) and summation of P_e with probability of parasitic absorption ($P = P_e + P_a$) are known.[22,28,63] Reproducing this relationship,

© 2024 The Author(s). Advanced Energy Materials published by Wiley-VCH GmbH
16146840, 0, Downloaded from https://onlinelibrary.wiley.com/doi/10.1002/aenm.202400965 by Cochrane Netherlands, Wiley Online Library on [14/08/2024]. See the Terms and Conditions (https://onlinelibrary.wiley.com/terms-and-conditions) on Wiley Online Library for rules of use; OA articles are governed by the applicable Creative Commons License

16146840, 0, Downloaded from https://onlinelibrary.wiley.com/doi/10.1002/aenm.202400965 by Cochrane Netherlands, Wiley Online Library on [14/08/2024]. See the Terms and Conditions (https://onlinelibrary.wiley.com/terms-and-conditions) on Wiley Online Library for rules of use; OA articles are governed by the applicable Creative Commons License

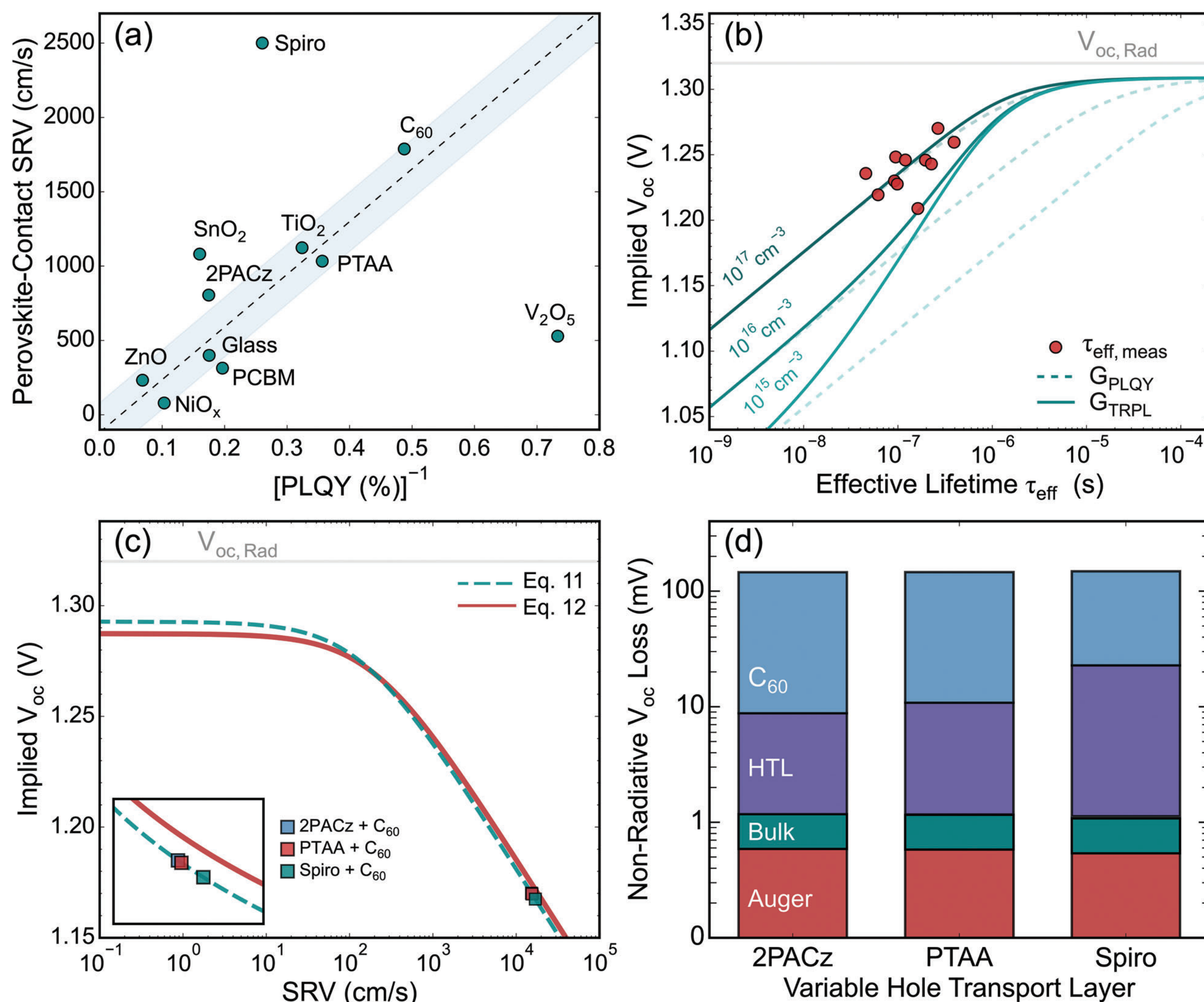

Figure 4. a) SRV plotted against the inverse PLQY of 11 contacts, in which the contacts were deposited on the rear of the unencapsulated perovskite film. b) Calculated implied open-circuit voltage using Equation (11) for different doping densities of $N_A = 10^{15}$, 10^{16}, and 10^{17} cm^{-3}. The solid line represents the carrier generation under TRPL conditions. For reference, the dashed line corresponds to the PLQY carrier generation rates in this work; $G_{PLQY} = 2.24 \times 10^{14}$ cm^{-3}s^{-1}. The radiative limit is also indicated with the solid gray line, $V_{oc,Rad} = 1.32$V. c) Plotting iV_{oc} as a function of SRV $= S_1 + S_2$ for $N_A = 10^{17}$ cm^{-3} and $\tau_{bulk} = 2$ µs. The green dashed line corresponds to iV_{oc} determination from the first discussed method, and the red solid line corresponds to the curve determined from the J_0 method. Inset: zoomed region which resolve the marker positions of the three hypothetical solar cell configurations. d) Visualization of the total non-radiative iV_{oc} losses for the three solar cell configurations, solved by determining the ratio of the total voltage loss due to each J_0 term (note that the losses are presented on a logarithmic voltage scale).

$iV_{oc} = V_{oc,\,Rad} + V_{therm}\ln(Q)$, where Q is defined as the external luminescence quantum efficiency;

$$Q = \frac{2k_{Rad}P_e\tau_{eff}(N_A + G\tau_{eff})}{1 + k_{Rad}\tau_{eff}P(N_A + 2G\tau_{eff}) + \tau_{eff}\sqrt{4Gk_{Rad}P + \frac{(1+k_{Rad}N_AP\tau_{eff})^2}{\tau_{eff}^2}}} \quad (11)$$

In this analysis, voltage losses due to Auger recombination are neglected. Based on the TRPL fluence conditions in our work, we set $G \approx 4.2 \times 10^{18}$ cm^{-3}s^{-1}, which we determine from the absorbed photon flux and perovskite thickness. The radiative recombination coefficient is set as $k_{Rad} = 2.9 \times 10$ cm^{-3}s^{-1}, which, as it has been shown, agrees with the carrier-dependent lifetime trend of the perovskite in Figure 1d and agrees with previous reports.[38] Following realistic literature values, we set P_e to be 0.13 and P_a to be 0.07.[64–67] With these parameters and measuring the perovskite bandgap to be $E_g = 1.6$ eV, we plot the iV_{oc} as a function of effective minority carrier lifetime for three different doping densities in Figure 4b.[68] For reference, the experimentally measured effective carrier lifetimes and the corresponding iV_{oc} derived from PLQY are plotted in the same figure. Accounting for the differences in carrier generation rates between the measurements (solid versus dashed lines), the implication from the position of the experimental data is that the background doping density of the triple cation perovskite used in this work is on the order of $10^{16} - 10^{17}$ cm^{-3}. Furthermore, as shown at

© 2024 The Author(s). Advanced Energy Materials published by Wiley-VCH GmbH

sufficiently high effective lifetimes, the maximum achievable V_{oc} is ≈11 mV below that of the radiative limit; this is a consequence of the notably strong influence of parasitic absorption (absorbing 7% of the total incoming light) in such high-quality hypothetical devices.

Of course, the corresponding open-circuit voltages for the plotted samples do not correlate to true device parameters, as these are half-stack samples and contain only one transport layer of interest. However, as we have already predetermined τ_{bulk} and the SRVs of several contacts of interest in their relevant configuration in the stack, we can combine Equations (11) and (10) and can estimate the upper limit to the open-circuit voltage for full device stacks, assuming that losses beyond the transport layers are negligible. Using $\tau_{bulk} = 2$ µs, we plot the iV_{oc} as a function of SRV = $S_1 + S_2$, shown as the green dashed line Figure 4c. It is evident that at SRVs beyond ≈100 cms^{-1}, surface recombination limits the iV_{oc}. At negligibly low SRV values, the total non-radiative iV_{oc} loss is 27 mV. The 27 mV loss in this case is due to both parasitic absorption, as described above, and to bulk recombination within the sample; this is effectively the iV_{oc} limit in which $\tau_{bulk} = \tau_{eff} = 2$ µs.

In the same figure, we also indicate the predicted open-circuit voltages for three different pin solar cell configurations, in which C_{60} is the common ETL and with different HTLs, namely 2PACz, PTAA and Spiro. As expected from the previously shown exceedingly high SRV of the perovskite-C_{60} interface, we see that in all cases C_{60} accounts for an additional voltage loss of 127 mV. This interface is clearly the voltage-limiting component in each hypothetical device. This limitation has been observed in other works using different methods; within the past two years, there has been a heightened focus in the perovskite community to understand and to mitigate the observed losses at the C_{60}-perovskite interface.[59,69,70] Additional losses due to the HTL are consequently minimal, as evident by the proximity of the markers. This of course does not imply that they do not limit the device in any way; should C_{60} be replaced with a highly passivating ETL, one finds that the HTL in each case then becomes the limiting point of recombination, which is evident from simply following the trend in Figure 4c.

We now consider the second and more generalized variation to predict iV_{oc} and estimate the voltage losses at each region of the device. From the SRH recombination parameters calculated in previous sections, it is also possible to make an estimation of the recombination parameter J_0, the reverse saturation current density.[62] J_0 is widely used in silicon PV as an assessment parameter of the silicon (half-fabricate) wafer; J_0 is notably automatically calculated in the Sinton WCT-120 analysis software and the value is generally returned with the lifetime and the iV_{oc}.[18,19] The benefit of using J_0 is that each loss component can simply be added up to determine the total dark recombination current density: $J_{0,\,tot} = J_{0,\,Rad} + J_{0,\,surf} + J_{0,\,bulk} + J_{0,\,Auger}$. This makes the determination of the key loss mechanisms relatively more straightforward than using Equation (11). The total iV_{oc} can then be simply determined using the standard expression:

$$iV_{oc} = V_{therm} \ln\left(\frac{J_{sc}}{J_{0,tot}}\right) \tag{12}$$

For the perovskite bandgap of 1.6 eV, $J_{0,Rad} = 1.43 \times 10^{-27}$ Acm^{-2} (we supply the solved equation between $J_{0,Rad}$ and E_g in the Supporting Information). We once more draw inspiration from silicon methods to convert τ_{bulk} into a reasonable estimation for $J_{0,bulk}$:[40]

$$J_{0,bulk} = \frac{W_{pvk}}{\tau_{bulk}} \frac{qn_i^2}{N_A + \Delta n} \tag{13}$$

It similarly follows that for surface recombination, with $S = S_1 + S_2$, that:[71]

$$J_{0,surf} = \frac{S}{2} \frac{qn_i^2}{N_A + \Delta n} \tag{14}$$

For a generalized SRH expression, each of the above bulk and surface components can simply be summed: $J_{0,\,eff} = J_{0,\,bulk} + J_{0,\,surf}$. The intrinsic carrier concentration for this perovskite is calculated to be $n_i = 7.03 \times 10^4$ cm^{-3} (see the Supporting Information for the calculation). As with the first variation, we also account for the probabilities of escape and of parasitic absorption by scaling the J_0 components accordingly. We account for the probability of emission by scaling the non-radiative J_0 terms with the inverse of P_e and by scaling the radiative J_0 term with P/P_e.[28] Using this approach, we determine $J_{0,bulk} = 1.90 \times 10^{-24}$ Acm^{-2}. While the Auger recombination is neglected in Equation (11), we show that it can easily be implemented in this generalized approach to predict a more accurate open-circuit voltage. Using an Auger coefficient of $C_{Auger} = 5 \times 10^{-29}$ cm^{-6}s^{-1}, we calculate $J_{0,Auger} = 1.90 \times 10^{-24}$ Acm^{-2}.[38] We argue it is good practice to incorporate the losses due to Auger, should high injection levels be required or applied in different measurements and test conditions, as is the case in this work. The predicted open-circuit voltage determined from Equation (12) is plotted as the red solid line in Figure 4c. Indeed, the difference in the green and red curves at low SRVs is the effect of including Auger in the latter variation. Auger accounts for an additional iV_{oc} loss of 5 mV (this is the difference in the plateaus of the curves at low SRVs in Figure 4c). Otherwise, the similarities between the solid and dashed curves emphasizes the minimal differences in the calculation variations to convert the SRH lifetime properties to predicted open-circuit voltages.

To emphasize the benefit in resolving each J_0 component, we visualize the extent of open-circuit voltage loss, due to Auger, bulk SRH and each of the perovskite-contact interfaces for the three hypothetical cells in Figure 4d. The extent of the iV_{oc} loss, which is logarithmically visualized along the y-axis, is calculated by assessing the relative contribution that each non-radiative recombination process has upon to the total non-radiative component of J_0. The benefit of this visualization is that relative contributions from non-limiting contacts can also be clearly resolved, rather than by simply noting the further minor losses as in Figure 4c. Inspecting the scale of Figure 4d highlights that in all cases, ≈90% of the total non-radiative iV_{oc} losses is due to the limiting perovskite-C_{60} interface. Evidently, to further improve the implied open-circuit voltage of these configurations, some ETL addition or substitution is required. However, we note that as each of these losses are derived from the percentage of the total non-radiative recombination, reducing, for example, the surface recombination at the C_{60} contact will in turn increase the relative contribution

© 2024 The Author(s). Advanced Energy Materials published by Wiley-VCH GmbH

16146840, 0, Downloaded from https://onlinelibrary.wiley.com/doi/10.1002/aenm.202400965 by Cochrane Netherlands, Wiley Online Library on [14/08/2024]. See the Terms and Conditions (https://onlinelibrary.wiley.com/terms-and-conditions) on Wiley Online Library for rules of use; OA articles are governed by the applicable Creative Commons License

16146840, 0, Downloaded from https://onlinelibrary.wiley.com/doi/10.1002/aenm.202400965 by Cochrane Netherlands, Wiley Online Library on [14/08/2024]. See the Terms and Conditions (https://onlinelibrary.wiley.com/terms-and-conditions) on Wiley Online Library for rules of use; OA articles are governed by the applicable Creative Commons License

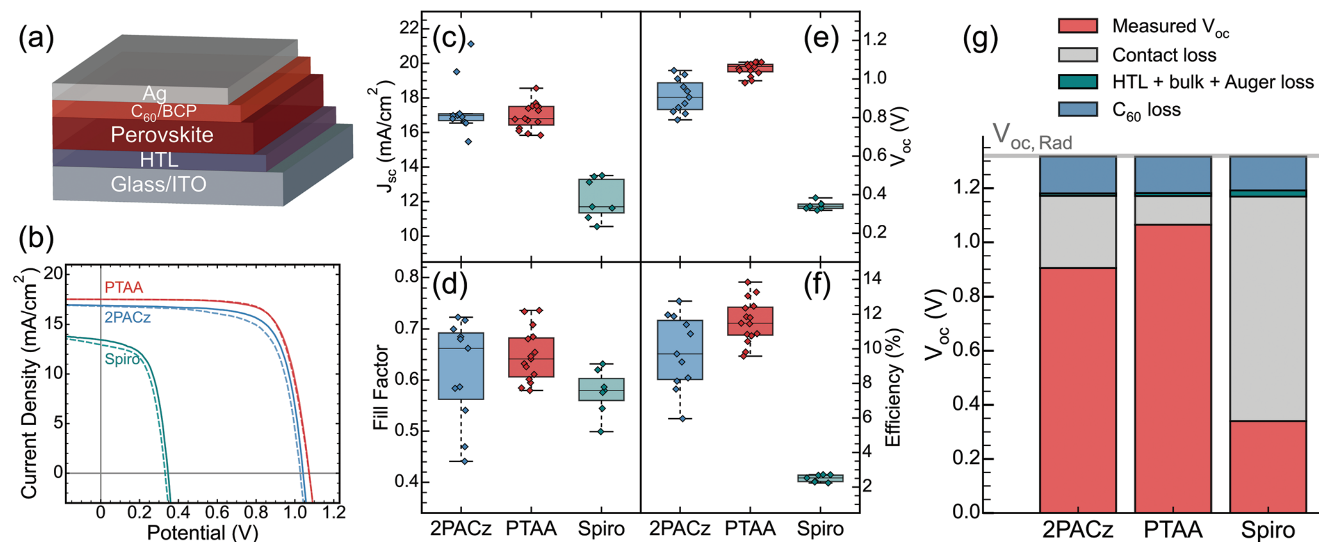

Figure 5. a) Schematic of pin stack, with variable HTLs, fabricated in this work. b) Measured light JV curves the devices, using PTAA (red), 2PACz (blue) and Spiro-OMeTAD (green) as the different hole transport layers. The solid and dashed lines represent the forward and reverse scans, respectively. c–f) Corresponding JV cell statistics of the tested devices. g) The complete breakdown of the measured open-circuit voltage and the resolved photovoltage losses for each of the tested device configurations in this work. Resolving each loss highlights the combined detrimental effects of the C_{60} interface and recombination issues beyond the transport layers (contact losses), compared to losses due to bulk, Auger and HTL recombination losses.

in other non-radiative loss mechanisms. Therefore, in order to optimize contacts for full devices, one requires information from both Figure 4c,d to understand the full picture of the stack.

We highlight that applying an optical assessment like the procedure described here is already a proven technique to optimize the photovoltage in perovskite solar cells. A notable example is shown in the work of Ginger and co-workers, where (3-aminopropyl)trimethoxysilane (APTMS) was applied as a passivating layer between the perovskite and the C_{60} interface. The group measured more than an order of magnitude reduction in the SRV when the APTMS layer was added compared to the perovskite/C_{60} control, corresponding to a 100 mV improvement in the iV_{oc} and a 60 mV increase in the measured V_{oc}. The advantage of the prior optical assessment is clearly showcased in this work, as the characterization ultimately led to a cell efficiency enhancement from 15.9% to >18%.[72,73]

Finally, we compare our open-circuit voltage predictions with fully fabricated devices. We prepare three different test device configurations, which are schematically shown in **Figure** 5a. As with our hypothetical devices, we only vary the HTL in each of the tested cells. The corresponding light JV curves for each of the three devices are shown in Figure 5b, with device statistics presented in Figure 5c–f. Notably, the open-circuit voltages extracted from the JV curves are significantly lower than the implied open-circuit voltages as calculated above. The differences in the median V_{oc} with the iV_{oc} for the 2PACz-, PTAA- and Spiro-based devices are 267, 106, and 829 mV, respectively. With the exception of the PTAA-based device, V_{oc} losses from factors that we have not yet accounted for are substantially higher than losses simply from non-radiative recombination in and at the interface of the perovskite film (Figure 5g). The poor device performances and JV parameters justify the argument that analyzing the device statistics alone may result in the erroneous conclusion that the low J_{sc} combined with lower than anticipated V_{oc} may be a consequence of high recombination at the perovskite-contact interface, or indeed due to high recombination rates within the bulk of the film. As we have shown with the long τ_{bulk} and high PLQY, it is not the bulk quality that is influencing the device performance, nor the interfaces that can account for such extensive losses. Therefore, some additional loss mechanisms are occurring beyond the photoactive layer. The device resistances extracted from the JV curves and from fitting the curves to the ideal diode equation notably show detrimentally low shunt resistances in both the 2PACz-based and Spiro-based cells ($R_{sh,2PACz}$ ≈2.5 KΩcm², $R_{sh,Spiro}$ ≈0.3 KΩcm²), while all devices suffer losses due to high series resistances ($R_{s,2PACz}$ ≈6 Ωcm², $R_{s,PTAA}$ ≈12 Ωcm², $R_{s,Spiro}$ ≈5.5 Ωcm²). We further explore the loss mechanisms based on the extracted resistances, and discuss optimization strategies in the Supporting Information. Notably, we find that the device performances are likely due to poor carrier mobilities in the transport layers.

5. Conclusion

In summary, we have shown that simple thickness-dependent effective lifetime measurements of perovskite half-stacks can resolve the total SRH recombination losses, within the perovskite bulk and at both interfaces. We have drawn upon established silicon assessment methods to quantify the resolved SRH recombination processes in terms of τ_{bulk} and SRV, experimentally determined the SRVs of 18 different contacts and confirmed our findings with supplemental PLQY characterization. Extending this analytical framework to full perovskite stacks relevant for photovoltaics, we find that C_{60}, while still possibly the most popular ETL in perovskite photovoltaics, accounts for ≈90% of the total non-radiative losses within the photoactive layer in typical device configurations. We present how the SRH parameters can be combined and converted to obtain an upper limit to the open-circuit voltage for effectively any device configuration. Despite the high

 © 2024 The Author(s). Advanced Energy Materials published by Wiley-VCH GmbH

SRV of C_{60}, we show that archetypal devices containing common HTLs such as 2PACz and PTAA can in principle achieve implied open-circuit voltages beyond 1.15 V. We furthermore highlight that solving for the iV_{oc} using the common recombination parameter J_0 enables one to neatly resolve and visualize not only each SRH recombination process, but also the influence of Auger at relevant injection levels. We emphasize that using this framework in addition to fabricating full devices can lead to a much stronger insight into device losses. We have evidently shown that even with a high quality perovskite film (τ_{bulk} = 2 μs) and reasonable perovskite interfaces, efficiencies of full devices can remain low due to detrimental processes beyond the photoactive layer. In our case, we note that the predominant losses likely arise from poor mobilities in the transport layers, or indeed simply a poor connection to the electrodes and external circuit. With the framework proposed, device optimization can be easily directed to the relevant limiting processes that may have been otherwise overlooked.

Supporting Information

Supporting Information is available from the Wiley Online Library or from the author.

Conflict of Interest

The authors declare no conflict of interest.

Author Contributions

S.C.G. fabricated and measured the lifetime, XRD, PL, UV-VIS, SEM, and some PLQY of the perovskite samples, measured the lifetime of the silicon illustrative example, fabricated and measured the solar cells, conducted the analysis and wrote the manuscript. J.G. measured the carrier diffusion length of the perovskite using SSPG and provided feedback with the manuscript. J.S.B. measured some PLQY of perovskite samples. J.A. fabricated the silicon illustrative sample. B.L.J.G., G.C., and E.C.G. provided experimental and analytical advice, feedback relating to the interpretation of the results and reviewed the manuscript.

Data Availability Statement

The data that support the findings of this study are available from the corresponding author upon reasonable request.

Keywords

J_0, perovskite, solar cell engineering, SRV

Received: March 1, 2024
Revised: May 23, 2024
Published online:

[1] M. Green, E. Dunlop, M. Yoshita, N. Kopidakis, K. Bothe, G. Siefer, X. Hao, *Prog. Photovoltaics* **2023**, *31*, 651.
[2] Y. Zhao, F. Ma, Z. Qu, S. Yu, T. Shen, H.-X. Deng, X. Chu, X. Peng, Y. Yuan, X. Zhang, J. You, *Science* **2022**, *377*, 531.
[3] W. Shockley, H. J. Queisser, *J. Appl. Phys.* **2004**, *32*, 510.
[4] A. Polman, M. Knight, E. C. Garnett, B. Ehrler, W. C. Sinke, *Science* **2016**, *352*, aad4424.
[5] J. Yoo, G. Seo, M. Chua, T. G. Park, Y. Lu, F. Rotermund, Y.-K. Kim, C. Moon, N. Jeon, J.-P. Correa-Baena, V. Bulovic, S. S. Shin, M. Bawendi, J. Seo, *Nature* **2021**, *590*, 587.
[6] Q. Jiang, J. Tong, R. Scheidt, X. Wang, A. Louks, Y. Xian, R. Tirawat, A. Palmstrom, M. Hautzinger, S. Harvey, S. Johnston, L. Schelhas, B. Larson, E. Warren, M. Beard, J. Berry, Y. Yan, K. Zhu, *Sci. (New York, N.Y.)* **2022**, *378*, 1295.
[7] M. J. Jeong, C. S. Moon, S. Lee, J. M. Im, M. Y. Woo, J. H. Lee, H. Cho, S. W. Jeon, J. H. Noh, *Joule* **2023**, *7*, 112.
[8] M. Degani, Q. An, M. Albaladejo-Siguan, Y. J. Hofstetter, C. Cho, F. Paulus, G. Grancini, Y. Vaynzof, *Sci. Adv.* **2021**, *7*, eabj7930.
[9] H. Sun, S. Gillespie, S. A. Rigter, J. S. van der Burgt, K. Datta, E. C. Garnett, *Adv. Mater. Technol.* **2023**, *8*, 2300241.
[10] R. Sinton, A. Cuevas, M. Stuckings, in *Conference Record of the Twenty Fifth IEEE Photovoltaic Specialists Conference - 1996*, IEEE, Piscataway, NJ **1996**, pp. 457–460.
[11] A. Cuevas, D. Macdonald, *Solar Energy* **2004**, *76*, 255.
[12] K. McIntosh, R. Sinton, in *Proceedings of the 23rd European Photovoltaic Solar Energy Conference Exhibition* Valencia, Spain, **2008**, pp. 77–82.
[13] H. D. Nagel, C. Berge, A. G. Aberle, *J. Appl. Phys.* **1999**, *86*, 6218.
[14] E. Yablonovitch, D. L. Allara, C. C. Chang, T. Gmitter, T. B. Bright, *Phys. Rev. Lett.* **1986**, *57*, 249.
[15] F. Wolny, M. Müller, A. Krause, D. Neuhaus, *Energy Procedia* **2017**, *124*, 235.
[16] T. Niewelt, B. Steinhauser, A. Richter, B. Veith-Wolf, A. Fell, B. Hammann, N. Grant, L. Black, J. Tan, A. Youssef, J. Murphy, J. Schmidt, M. Schubert, S. Glunz, *Sol. Energy Mater. Sol. Cells* **2022**, *235*, 111467.
[17] A. Cuevas, R. A. Sinton, *Prog. Photovoltaics* **1997**, *5*, 79.
[18] A. Kimmerle, P. Rothhardt, A. Wolf, R. A. Sinton, *Energy Procedia* **2014**, *55*, 101.
[19] A. Kimmerle, J. Greulich, A. Wolf, *Sol. Energy Mater. Sol. Cells* **2015**, *142*, 116.
[20] A. Sproul, *J. Appl. Phys.* **1994**, *76*, 2851.
[21] M. Saliba, T. Matsui, J.-Y. Seo, K. Domanski, J.-P. Correa-Baena, M. K. Nazeeruddin, S. M. Zakeeruddin, W. Tress, A. Abate, A. Hagfeldt, M. Grätzel, *Energy Environ. Sci.* **2016**, *9*, 1989.
[22] L. M. Pazos-Outón, T. P. Xiao, E. Yablonovitch, *J. Phys. Chem. Lett.* **2018**, *9*, 1703.
[23] T. Sherkar, C. Momblona, L. Gil-Escrig, J. Ávila, M. Sessolo, H. Bolink, L. Koster, *ACS Energy Lett.* **2017**, *2*, 1214.
[24] D. Luo, R. Su, W. Zhang, Q. Gong, R. Zhu, *Nat. Rev. Mater.* **2020**, *5*, 44.
[25] M. Müller, *Energy Procedia* **2016**, *92*, 138.
[26] A. Richter, S. W. Glunz, F. Werner, J. Schmidt, A. Cuevas, *Phys. Rev. B* **2012**, *86*, 165202.
[27] D. Phillips, R. Drake, D. OConnor, R. Christensen, *Instrum. Sci. Technol.* **1985**, *14*, 267.
[28] T. Kirchartz, J. A. Márquez, M. Stolterfoht, T. Unold, *Adv. Energy Mater.* **2020**, *10*, 1904134.
[29] L. Kudriashova, D. Kiermasch, P. Rieder, M. Campbell, K. Tvingstedt, A. Baumann, G. Astakhov, V. Dyakonov, *J. Phys. Chem. Lett.* **2017**, *8*, 4698.
[30] Y. Yuan, G. Yan, C. Dreessen, T. Rudolph, M. Hülsbeck, B. Klingebiel, J. Ye, U. Rau, T. Kirchartz, *Nat. Mater.* **2024**, *23*, 391.
[31] W. Chen, N. Pham, H. Wang, B. Jia, X. Wen, *ACS Appl. Mater. Interfaces* **2021**, *13*, 5752.
[32] P. Chen, Y. Xiao, L. Li, L. Zhao, M. Yu, S. Li, J. Hu, B. Liu, Y. Yang, D. Luo, C.-H. Hou, X. Guo, J.-J. Shyue, Z.-H. Lu, Q. Gong, H. J. Snaith, R. Zhu, *Adv. Mater.* **2023**, *35*, 2206345.

© 2024 The Author(s). Advanced Energy Materials published by Wiley-VCH GmbH

16146840, 0, Downloaded from https://onlinelibrary.wiley.com/doi/10.1002/aenm.202400965 by Cochrane Netherlands, Wiley Online Library on [14/08/2024]. See the Terms and Conditions (https://onlinelibrary.wiley.com/terms-and-conditions) on Wiley Online Library for rules of use; OA articles are governed by the applicable Creative Commons License

[33] A. Ren, H. Lai, X. Hao, Z. Tang, H. Xu, B. Yu Jeco-Espaldon, K. Watanabe, L. Wu, M. Sugiyama, J. Wu, D. Zhao, *Joule* **2020**, *4*, 1263.
[34] B. Krogmeier, F. Staub, D. Grabowski, U. Rau, T. Kirchartz, *Sustainable Energy Fuels* **2018**, *2*, 1027.
[35] L. Krückemeier, B. Krogmeier, Z. Liu, U. Rau, T. Kirchartz, *Adv. Energy Mater.* **2021**, *11*, 2003489.
[36] A. Al-Ashouri, E. Köhnen, B. Li, A. Magomedov, H. Hempel, P. Caprioglio, J. A. Márquez, A. B. M. Vilches, E. Kasparavicius, J. A. Smith, N. Phung, D. Menzel, M. Grischek, L. Kegelmann, D. Skroblin, C. Gollwitzer, T. Malinauskas, M. Jošt, G. Matič, B. Rech, R. Schlatmann, M. Topič, L. Korte, A. Abate, B. Stannowski, D. Neher, M. Stolterfoht, T. Unold, V. Getautis, S. Albrecht, *Science* **2020**, *370*, 1300.
[37] M. Liu, S. Dahlström, C. Ahläng, S. Wilken, A. Degterev, A. Matuhina, M. Hadadian, M. Markkanen, K. Aitola, A. Kamppinen, J. Deska, O. Mangs, M. Nyman, P. Lund, J.-H. Smått, R. Österbacka, P. Vivo, *J. Mater. Chem. A* **2022**, *10*, 11721.
[38] C. M. Wolff, S. A. Bourelle, L. Q. Phuong, J. Kurpiers, S. Feldmann, P. Caprioglio, J. A. Marquez, J. Wolansky, T. Unold, M. Stolterfoht, S. Shoaee, F. Deschler, D. Neher, *Adv. Energy Mater.* **2021**, *11*, 2101823.
[39] I. Allegro, Y. Li, B. S. Richards, U. W. Paetzold, U. Lemmer, I. A. Howard, *J. Phys. Chem. Lett.* **2021**, *12*, 2293.
[40] T. P. Weiss, B. Bissig, T. Feurer, R. Carron, S. Buecheler, A. N. Tiwari, *Sci. Rep.* **2019**, *9*, 5385.
[41] E. Aydin, M. De Bastiani, S. De Wolf, *Adv. Mater.* **2019**, *31*, 1900428.
[42] J. Wang, W. Fu, S. Jariwala, I. Sinha, A. Jen, D. Ginger, *ACS Energy Lett.* **2018**, *4*, 222.
[43] R. Brenes, D. Guo, A. Osherov, N. K. Noel, C. Eames, E. M. Hutter, S. K. Pathak, F. Niroui, R. H. Friend, M. S. Islam, H. J. Snaith, V. Bulović, T. J. Savenije, S. D. Stranks, *Joule* **2017**, *1*, 155.
[44] Y. Chen, H. T. Yi, X. Wu, R. Haroldson, Y. Gartstein, Y. Rodionov, K. Tikhonov, A. Zakhidov, X. Zhu, V. Podzorov, *Nat. Commun.* **2016**, *7*, 12253.
[45] Q. Dong, Y. Fang, Y. Shao, P. Mulligan, J. Qiu, L. Cao, J. Huang, *Science* **2015**, *347*, 967.
[46] T. Savenije, C. Ponseca, L. Kunneman, M. Abdellah, K. Zheng, Y. Tian, Q. Zhu, S. Canton, I. Scheblykin, T. Pullerits, A. Yartsev, V. Sundström, *J. Phys. Chem. Lett.* **2014**, *5*, 2189.
[47] C. Wehrenfennig, G. E. Eperon, M. B. Johnston, H. J. Snaith, L. M. Herz, *Adv. Mater.* **2014**, *26*, 1584.
[48] G. Xing, N. Mathews, S. Sun, S. S. Lim, Y. M. Lam, M. Grätzel, S. Mhaisalkar, T. C. Sum, *Science* **2013**, *342*, 344.
[49] Y. Yang, M. Yang, T. Moore, David, Y. Yan, E. Miller, K. Zhu, M. Beard, *Nat. Energy* **2017**, *2*, 16207.
[50] S. D. Stranks, G. E. Eperon, G. Grancini, C. Menelaou, M. J. P. Alcocer, T. Leijtens, L. M. Herz, A. Petrozza, H. J. Snaith, *Science* **2013**, *342*, 341.
[51] G. Adhyaksa, S. Brittman, H. Abolins, A. Lof, X. Li, J. Keelor, Y. Luo, T. Duevski, R. Heeren, S. Ellis, D. Fenning, E. Garnett, *Adv. Mater.* **2018**, *30*, 1804792.
[52] H. P. Pasanen, P. Vivo, L. Canil, H. Hempel, T. Unold, A. Abate, N. V. Tkachenko, *J. Phys. Chem. Lett.* **2020**, *11*, 445.
[53] D. deQuilettes, S. Koch, S. Burke, R. Paranji, A. Shropshire, M. Ziffer, D. Ginger, *ACS Energy Lett.* **2016**, *1*, 438.
[54] A. Palechor, J. Caram, P. Hierrezuelo-Cardet, F. Ventosinos, D. Pérez del Rey, H. Bolink, J. Schmidt, *Energy Technol.* **2023**, *11*, 2200814.
[55] C. C. Boyd, R. C. Shallcross, T. Moot, R. Kerner, L. Bertoluzzi, A. Onno, S. Kavadiya, C. Chosy, E. J. Wolf, J. Werner, J. A. Raiford, C. de Paula, A. F. Palmstrom, Z. J. Yu, J. J. Berry, S. F. Bent, Z. C. Holman, J. M. Luther, E. L. Ratcliff, N. R. Armstrong, M. D. McGehee, *Joule* **2020**, *4*, 1759.
[56] J. Holovský, E. Horynová, L. Horák, K. Ridzoňová, Z. Remeš, L. Landová, R. K. Sharma, *Vacuum* **2021**, *194*, 110613.
[57] Y. Wang, L. Duan, M. Zhang, Z. Hameiri, X. Liu, Y. Bai, X. Hao, *Solar RRL* **2022**, *6*, 2200234.
[58] M. Saliba, J.-P. Correa-Baena, C. Wolff, M. Stolterfoht, N. Phung, S. Albrecht, D. Neher, A. Abate, *Chem. Mater.* **2018**, *30*, 4193.
[59] J. Warby, F. Zu, S. Zeiske, E. Gutierrez-Partida, L. Frohloff, S. Kahmann, K. Frohna, E. Mosconi, E. Radicchi, F. Lang, S. Shah, F. Peña-Camargo, H. Hempel, T. Unold, N. Koch, A. Armin, F. De Angelis, S. D. Stranks, D. Neher, M. Stolterfoht, *Adv. Energy Mater.* **2022**, *12*, 2103567.
[60] L. Nakka, Y. Cheng, A. G. Aberle, F. Lin, *Adv. Energy Sustainability Res.* **2022**, *3*, 2200045.
[61] S. Olthof, K. Meerholz, *Sci. Rep.* **2017**, *7*, 40267.
[62] A. Cuevas, *Energy Procedia* **2014**, *55*, 53.
[63] T. Kirchartz, *J. Phys. Chem. Lett.* **2019**, *10*, 5892.
[64] J. M. Richter, M. Abdi-Jalebi, A. Sadhanala, M. Tabachnyk, J. P. Rivett, L. M. Pazos-Outón, K. C. Gödel, M. Price, F. Deschler, R. H. Friend, *Nat. Commun.* **2016**, *7*, 13941.
[65] J. M. Ball, S. D. Stranks, M. T. Hörantner, S. Hüttner, W. Zhang, E. J. W. Crossland, I. Ramirez, M. Riede, M. B. Johnston, R. H. Friend, H. J. Snaith, *Energy Environ. Sci.* **2015**, *8*, 602.
[66] Y. Da, Y. Xuan, Q. Li, *Sol. Energy Mater. Sol. Cells* **2018**, *174*, 206.
[67] D.-L. Wang, H.-J. Cui, G.-J. Hou, Z.-G. Zhu, Q.-B. Yan, G. Su, *Sci. Rep.* **2016**, *6*, 18922.
[68] P. Makuła, M. Pacia, W. Macyk, *J. Phys. Chem. Lett.* **2018**, *9*, 6814.
[69] D. Menzel, A. Al-Ashouri, A. Tejada, I. Levine, J. A. Guerra, B. Rech, S. Albrecht, L. Korte, *Adv. Energy Mater.* **2022**, *12*, 2201109.
[70] F. Ye, S. Zhang, J. Warby, J. Wu, E. Gutierrez-Partida, F. Lang, S. Shah, E. Saglamkaya, B. Sun, F. Zu, S. Shoaee, H. Wang, B. Stiller, D. Neher, W.-H. Zhu, M. Stolterfoht, Y. Wu, *Nat. Commun.* **2022**, *13*, 7454.
[71] L. E. Black, *Surface Recombination Theory*, Springer International Publishing, Cham, **2016**, pp. 15–28.
[72] Y. Shi, E. Rojas-Gatjens, J. Wang, J. Pothoof, R. Giridharagopal, K. Ho, F. Jiang, M. Taddei, Z. Yang, E. M. Sanehira, M. D. Irwin, C. Silva-Acuña, D. S. Ginger, *ACS Energy Lett.* **2022**, *7*, 4081.
[73] S. Jariwala, S. Burke, S. Dunfield, R. C. Shallcross, M. Taddei, J. Wang, G. E. Eperon, N. R. Armstrong, J. J. Berry, D. S. Ginger, *Chem. Mater.* **2021**, *33*, 5035.

© 2024 The Author(s). Advanced Energy Materials published by Wiley-VCH GmbH

16146840, 0, Downloaded from https://onlinelibrary.wiley.com/doi/10.1002/aenm.202400965 by Cochrane Netherlands, Wiley Online Library on [14/08/2024]. See the Terms and Conditions (https://onlinelibrary.wiley.com/terms-and-conditions) on Wiley Online Library for rules of use; OA articles are governed by the applicable Creative Commons License